Materials Advances

ROYAL SOCIETY OF CHEMISTRY

PAPER

View Article Online
View Journal | View Issue

Cite this: *Mater. Adv.*, 2025, 6, 5940

Biomineralized metal–organic frameworks targeting collagen for suppression of myocardial fibrosis and enhancement of cardiac function

Jiao Liu, Xueli Zhao, Bo Wang, Ruoxuan Li, Yuze Qin, Yue Wang, Jia Zhao, Lanlan Zhang, Liang Yu* and Liwen Liu *

Myocardial fibrosis is a common pathological feature of numerous cardiovascular disorders, and plays a critical role in the development and progression of heart diseases. To address this, a novel delivery system (NH_2-UiO-66@Cur@PCM) based on a biomineralized metal–organic framework (MOF) was ingeniously designed and constructed by post-modification synthesis. Meanwhile, first-principles density functional theory (DFT) simulations have been employed to confirm that the process of drug molecules integrating into the MOF matrix lattice is spontaneous and there are strong hydrogen bonds. Furthermore, in order to demonstrate the intervention efficiency of NH_2-UiO-66@Cur@PCM *in vivo* under simulated myocardial fibrosis, NH_2-UiO-66@Cur@PCM was effectively internalized after systemic administration, which effectively improved the myocardial microenvironment of mice by limiting the combined effect of inflammation and myocardial collagen, thus achieving an overall improvement in the microenvironment of mice hearts. Overall, these findings provide a solid theoretical basis and a new research direction for the construction of an innovative MOF material platform and the exploration of cardiovascular disease treatment strategies.

Received 17th February 2025,
Accepted 23rd June 2025

DOI: 10.1039/d5ma00149h

rsc.li/materials-advances

1. Introduction

Myocardial fibrosis is a pathological manifestation of a variety of cardiovascular diseases, including but not limited to hypertrophy cardiomyopathy, diabetic cardiomyopathy, viral myocardium, myocardial infarction, and ischemic cardiomyopathy, among others.[1,2] It is of particular note that alterations in scar formation can result in detrimental effects on myocardial tissue, culminating in the manifestation of left ventricular dysfunction, which subsequently leads to the development of heart failure.[3,4] At present, β-blockers, ACEI/ARB and aldosterone antagonists commonly used in clinical practice can delay fibrosis by inhibiting sympathetic nerve and blocking RAAS, but they have many adverse reactions and are difficult to reverse the disease. Although the emerging stem cell therapy and gene therapy are innovative, they cannot be widely used due to the risk of stem cell tumorigenesis and gene carrier delivery problems.[5,6] Therefore, researchers focus on natural products with multi-target regulation characteristics. Curcumin (Cur)[7,8] is a type of polyphenolic compound found in turmeric, a natural product with potent anti-fibrosis, anti-oxidation, and anti-inflammatory properties. Specifically, it can reduce myocardial collagen deposition, matrix metalloproteinase (MMP) activity and malondialdehyde levels, thereby contributing to its anti-fibrosis effect. However, its short half-life, poor gastrointestinal absorption, limited water solubility, and easy degradation under alkaline conditions result in reduced bioavailability, potentially limiting its clinical application.[9] Therefore, there is a pressing need to develop a targeted drug delivery system with sustained release effects that can protect drug molecules and enhance their bioavailability.[10,11]

As emerging drug carriers, metal–organic frameworks (MOFs) have experienced unprecedented development in the past few decades, bringing innovative prospects for drug delivery systems.[12] The high porosity and large specific surface area of MOFs provide distinct advantages in enhancing the loading efficiency of guest molecules, making them superior to other inorganic or organic materials.[13] The ability to more efficiently use drugs *in vivo* and recyclability can be increased by facile functionalization, and by their excellent biocompatibility, water solubility, and degradability.[14] More importantly, there are hydrogen bonding effects, van der Waals forces, π–π stacking between aromatic rings and other forces in MOFs. Therefore, MOFs are in the ascendant for drug delivery systems. NH_2-UiO-66 is a porous material with a unique structure based on $[Zr_6O_4(OH)_4]$ octahedral clusters.[15,16] This compound has unique chemical and physical properties, such as excellent

Department of Ultrasound, Xijing Hypertrophic Cardiomyopathy Center, Xijing Hospital, Fourth Military Medical University, Xi'an, Shaanxi 712000, China

water resistance, excellent chemical and thermal stability, remarkable biodegradability and high specific surface area. Therefore, this particular compound is an excellent candidate for encapsulating a variety of drugs.[8]

Herein, we developed a targeted nano-drug delivery system (NH_2-UiO-66@Cur@PCM) for delaying or preventing myocardial fibrosis by using a specifically recognized PCM peptide[17] (WLSEAGPVVTVRALRGTGSW) and functionalized NH_2-UiO-66. Furthermore, density functional theory (DFT) was employed to explore in depth the interaction mechanism between the MOF and Cur, and the key binding sites between them were identified, which provides a solid theoretical basis for the stability of nano-drugs and the optimization of drug loading. To verify the intervention effect of the nanoparticles, *in vivo* injection experiments revealed that the nanoparticles can effectively inhibit the progression of myocardial fibrosis and cardiomyocyte apoptosis in mice, ultimately improving cardiac function in mice and highlighting their application potential in classified treatment of cardiovascular diseases.

2. Materials and methods

2.1 Synthesis and characterization of NH_2-UiO-66@Cur@PCM

$ZrCl_4$ (0.8 mmol), 2-aminoterephthalic acid (0.5 mmol), and *N*,*N*-dimethylformamide (DMF) (30 mL) were mixed in a 100 mL Teflon-lined vessel at 25 °C and were stirred until a clear solution was obtained. Then, the temperature was set at 110° and the pressure was set at 40 atm in a microwave digestion instrument where the solution was kept and maintained for 6 hours, and the solution was cooled to ambient temperature. The solution was then centrifuged, and the resultant particles were soaked in 20 mL of chloroform for 5 days to exchange the residual DMF with chloroform, which also helped to eliminate any unreacted substances. Finally, the nanomaterial was kept in a vacuum drying oven at a temperature of 120 °C to ensure the complete elimination of any residual solvents.

PXRD data were obtained on a Bruker D8 ADVANCE X-ray powder diffractometer (Cu-Kα, 1.5418 Å). The morphology of NH_2-UiO-66 was explored by transmission electron microscopy (TEM) (Philips CM30). The size was examined by the dynamic light scattering (DLS) method. And the gas sorption isotherms were measured with ASAP 2020M adsorption equipment.

2.2 Molecular dynamics simulations

Here, we utilize density functional theory (DFT)[18] to investigate the intermolecular interactions between MOFs and drug molecules. The methodology utilized is based on the Vienna *ab initio* simulation package (VASP), which employs the generalized gradient approximation (GGA) and Perdew–Burke–Ernzerhof (PBE) exchange correlation potential.[19,20] Additionally, the DFT-D3 model of Grimme is modified by van der Waals interactions, with an energy cutoff value of 520 eV.[21] The structure is fully relaxed until the maximum force on each atom is less than 0.01 eV $Å^{-1}$, and the energy converges to 10^{-5} eV. The intermolecular graph (IGM) is obtained from the DFT-optimized periodic structure.[22]

2.3 Encapsulation of Cur into NH_2-UiO-66 and release studies

The Cur embedded in the NH_2-UiO-66 matrix was quantified using the complex obtained after centrifugation. The standard curve of Cur was drawn using a UV-visible spectrophotometer. The encapsulation efficiency of curcumin was calculated as follows: EE (%) = Cr/Ct × 100%, where Cr is the actual amount of drug encapsulated into nanoparticles and Ct is the total amount of drug input. To characterize the interaction between NH_2-UiO-66 and Cur, the release curve of Cur from the complex was examined using dialysis. The complex was dispersed in a dialysis bag (MW = 12 kDa) and immersed in 50 mL of PBS solution (PBS-SDS; 0.5% w/v, pH = 7.4 and 5.4), which was stirred at a constant temperature of 37 °C (50 rpm). Subsequently, 2 mL of dialysate was collected at specific time intervals, and fresh PBS was added to replace the previous solution. The concentration of Cur in the dialysate was determined using an UV-visible spectrophotometer.

2.4 Toxicity assessment

In order to evaluate the cytotoxicity, cardiac fibroblasts (CFs)[23] were first adhered to 96-well plates at a density of 5×10^3 cells per well, and then different concentrations (0, 6.25, 12.5, 25, 50, 100, and 200 μg mL^{-1}) of MOF solution were added to the well (n = 5). After 24 h of incubation, a 10% (v/v) cell counting kit reagent (CCK-8, Dojindo, Kumamoto, Japan) was added to all wells, and the reaction was carried out at 37 °C for 2 h in the dark. Finally, the solution was detected using a microplate reader at 450 nm.

2.5 Establishment of myocardial fibrosis model mice and grouping

Balb/c mice were randomly divided into four groups: the sham operation group (Sham group), the isoproterenol (ISO) stimulation group, the ISO + NH_2-UiO-66@Cur group, and the ISO + NH_2-UiO-66@Cur@PCM group, with five mice in each group: the mice were subcutaneously injected with 200 μL of isoproterenol (10 mg kg^{-1} day^{-1}) for 15 days to establish the myocardial fibrosis model and then treated for 15 days.[4,24,25] All animal experiments performed in this study strictly follow ''The NIH Guidelines On The Use Of Laboratory Animals'' and are approved by the Animal Welfare and Ethics Committee of the Laboratory Animal Centre of Fourth Military Medical University.

2.6 Echocardiography measurement

Ultrasound examination was performed on mice in different groups. After one month of treatment, the anterior chest area and left chest area of the mice were shaved and then placed in a supine position. Two-dimensional and M-mode echocardiography images were obtained using echocardiography. The left ventricular internal dimensions in systole (LVIDs) and diastole (LVIDd) were recorded. The left ventricular ejection fraction

(LVEF) and left ventricular fractional shortening (LVFS) were calculated according to the measured parameters.

2.7 Histopathology and immunohistochemistry for the heart

As previously reported by our research group,[26] the assessment of collagen deposition was performed *via* Masson trichrome staining. The procedure involves the excision of hearts, their subsequent fixation in a solution of 4% paraformaldehyde, and paraffin embedding for preservation. After embedding, the tissue was cut into 5 mm thick and Masson staining was performed on each tissue segment. The subsequent analysis was performed using digital image software specifically designed for this purpose, Image Pro Plus (Media Cybernetics, Bethesda, MD, USA). This computational analytical tool enabled the quantification of the fibrotic region *via* image processing techniques.

Immunohistochemistry analysis was performed on heart tissue sections to evaluate the expression of collagen-1 (Col-1) and collagen-3 (Col-3) proteins. The heart tissues were initially fixed, paraffin-embedded and subsequently sectioned into 4 μm slices. Deparaffinization and rehydration of the sections were carried out before antigen retrieval using the sodium citrate buffer. Nonspecific binding of the antibodies was blocked by incubating the sections with 10% normal goat serum for 1 h at room temperature. The sections were then exposed overnight at 4 °C to the primary antibodies. Finally, the sections were stained with the secondary antibodies and imaged using Image Pro Plus software.

2.8 Expression of the IL-6, CTGF, and Col-1 genes measured by real-time quantitative PCR (RT-qPCR)

The extracted pieces of LV tissue were subjected to RNA according to the kit instructions, and the purity and concentration of the RNA were subsequently determined by utilizing a microplate reader. The RNA was then reverse transcribed into cDNA, and the specific primers and the 7500 Fast Real-Time PCR System (Foster City, CA, USA) were employed for the RT-qPCR of the target gene. The expression level of the target gene was quantified using the C_t method, with β-actin mRNA serving as the internal reference. The specific primer names and sequences are provided in Table 1.

2.9 Statistical analysis

Statistical analysis and curve fitting were performed using GraphPad Prism 8; each experiment was repeated 3 times, data were expressed as means ± standard deviation. ANOVA was employed for group comparison; P values < 0.05 were considered statistically significant.

3. Results and discussion

3.1 Preparation and characterization of NH_2-UiO-66@Cur@PCM

In this study, we successfully synthesized MOF-based targeted nanomaterials, namely, NH_2-UiO-66@Cur@PCM. Firstly, NH_2-UiO-66 was synthesized by the microwave reaction in an ultra-fast way, which showed a higher yield and smaller particle size of the MOF material than the solvothermal method. Then, Cur was encapsulated into the MOF shell by a one-pot method, and PEG-PEI 25 K with high water solubility and biocompatibility was modified outside the shell. Finally, in order to improve the ability of nanoparticles to target the lesion area of myocardial fibrosis, the cardiac-targeting peptide PCM was conjugated to the surface of NH_2-UiO-66@Cur by the carbodiimide coupling method. Significantly, this way notably promotes the formation of covalent bonds, which is a highly controllable process for immobilizing biomolecules on the surface, thereby ensuring adequate stability for surfactants.

The PXRD spectrum of NH_2-UiO-66 is shown in Fig. 1a, and the main peaks of NH_2-UiO-66 (2θ = 7.42, 8.62 and 25.82°) are in good agreement with those of the previous X-ray diffraction spectra. These findings indicate that the structural integrity of NH_2-UiO-66, NH_2-UiO-66@Cur, and NH_2-UiO-66@Cur@PCM remains unaltered. The N_2 adsorption/desorption isotherms are presented in Fig. 1b; the specific adsorption capacity of NH_2-UiO-66 is reported to be 251 $cm^3\ g^{-1}$, and a decrease in the adsorption capacity of NH_2-UiO-66@Cur is observed, dropping to 201 $cm^3\ g^{-1}$ at 77 K. This evidence suggests the successful incorporation of Cur within the MOF structure. The maximum Cur EE in the synthesized MOF was studied and found to be 48.7 ± 6.3 (%). This value is larger than that reported,[8] which may be due to the slightly lower specific surface area of the MOF.

In addition, DLS analysis was developed for evaluating the hydrodynamic diameter of nanoparticles, considering the importance of the nanocomposite size in phagocytosis to target cells.[8,27] As is clearly evident from Fig. 1c, NH_2-UiO-66@Cur was found to exhibit an increased hydrodynamic diameter. The average diameters of NH_2-UiO-66, NH_2-UiO-66@Cur, and NH_2-UiO-66@Cur@PCM were determined to be 248 ± 9 nm, 269 ± 13 nm, and 331 ± 6 nm, respectively. Substantial augmentation in size after drug loading is primarily attributed to intermolecular entanglements like hydrogen bonds between the drugs and the nanocomposites.[28] The average surface zeta potentials were 30 ± 2 mV, 49 ± 3 mV and −12.9 ± 3 mV (Fig. 1d), respectively, which further indicated that Cur and PCM peptides were successfully connected and the negative surface charge of the nanoparticles prolongs their circulation in the bloodstream,

Table 1 Sequences of primers for RT-qPCR

	Forward primer (5′–3′)	Reverse primer (5′–3′)
β-actin	TCATCACTATTGGCAACGAGC	AACAGTCCGCCTAGAAGCAC
IL-6	CTTCCATCCAGTTGCCTTCT	CTCCGACTTGTGAAGTGGTATAG
Col-1	GACATGTTCAGCTTTGTGGACCTC	GGGACCCTTAGGCCATTGTGTA
CTGF	ACTATGATGCGAGCCAACTG	CTCCAGTCTGCAGAAGGTATTG

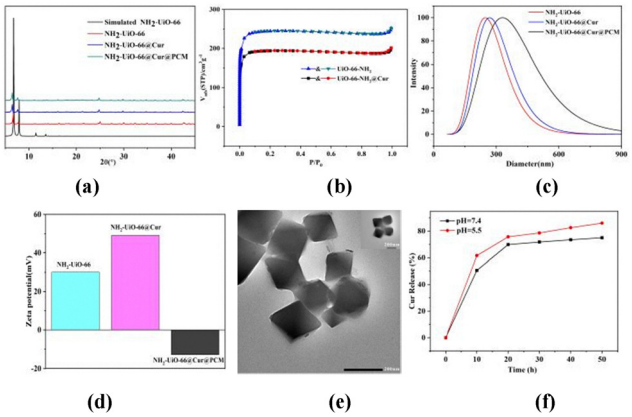

Fig. 1 (a) PXRD patterns of NH_2-UiO-66, NH_2-UiO-66@Cur and NH_2-UiO-66@Cur@PCM. (b) N_2 adsorption isotherm of NH_2-UiO-66 and NH_2-UiO-66@Cur. (c) Hydrodynamic size distribution of NH_2-UiO-66, NH_2-UiO-66@Cur and NH_2-UiO-66@Cur@PCM. (d) Zeta potential of NH_2-UiO-66, NH_2-UiO-66@Cur and NH_2-UiO-66@Cur@PCM. (e) TEM image of NH_2-UiO-66@Cur. (f) Cumulative release of Cur from NH_2-UiO-66@Cur in PBS with pH 5.5 and 7.4.

thereby reducing any cytotoxicity caused by the proton sponge effect.

The morphology of NH_2-UiO-66@Cur@PCM was characterized *via* TEM (Fig. 1e), the TEM image obviously demonstrated that the size distribution was uniform and a semi-symmetrical crystal structure with a triangular bottom cone shape was observed, which resembles those reported in previous literature. However, the size is larger than those reported in the literature, which may be due to the different pH values of the solution.[29] In order to explore the affinity between the adsorbent and the drug, the release characteristics of MOFs absorbed by Cur were studied in pH = 7.4 and acidified PBS solutions (pH = 5.5). As expected, the lower the pH value, the stronger the acidity, and the faster the Cur release in the drug-absorbing MOFs (Fig. 1f). Compared with UiO-66, NH_2-UiO-66 has a stronger interaction with Cur due to its stronger interaction between its functional groups and Cur, and has a greater interaction with drugs.[30] The result also indicates that it is stable at physiological pH, but degrades under acidic conditions, which can be attributed to the low-density functional groups in the skeleton and the acidic medium reducing the interaction between the drug and the skeleton.

The rate at which an adsorbate is adsorbed, as characterized by the adsorption kinetics, plays a crucial role in determining the overall efficiency of an adsorption system.[31] Through an adsorption process for 0–100 minutes, the influence of varying stirring times on the adsorption capacity of Cur by NH_2-UiO-66 was extensively studied and discussed (Fig. 2). Following an initial increase, the adsorption capacity (q_t) gradually decelerated and eventually reached a stable value after 100 minutes. Therefore, a 100-minute interval is chosen as the balance time.[32] In the initial stage of adsorption, the rapid adsorption equilibrium observed in the MOF can be attributed to the abundance of adsorption sites, uniformity of pores, and the

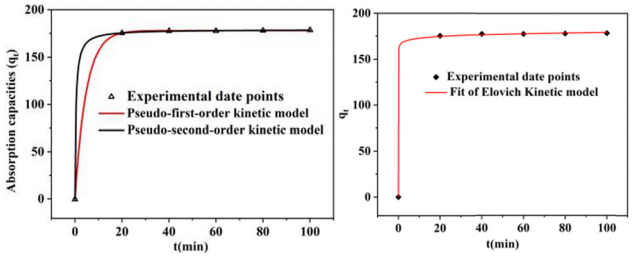

Fig. 2 Pseudo-first-order, pseudo-second-order and Elovich kinetic plots for Cur adsorption by the MOF.

expansive specific surface area present within the material, so it showed a higher adsorption rate in the first 10 minutes. As the reaction progresses, the adsorption sites become fewer and fewer, and there are a large number of positive charges on the surface. This will have a repulsive force on the free Cur in the solution, and the concentration gradient as the adsorption power becomes smaller and smaller slows down the adsorption rate.

Both pseudo-first-order and pseudo-second-order kinetics revealed a correlation coefficient of 0.99, indicating that the adsorption rate increased with the increase of the adsorbent concentration. In addition, the first-order kinetic model also implies that the adsorption sites are limited and the adsorption process is dynamic, that is, the adsorption rate is equal to the desorption rate. Furthermore, q_e calculated by the quasi-second-order kinetic model is close to the experimentally measured saturation adsorption capacity. The kinetic study confirms that the adsorption process follows second-order kinetics, underscoring that it is primarily dictated by chemical interactions rather than by transport steps. Active chemisorption can be described most effectively using the Elovich model. And the R^2 value was 0.99, indicating that there may be a chemical interaction between the drug and the MOF.

Modeling the kinetic data with pseudo-first-order, pseudo-second-order, and Elovich models, was achieved using three kinetic models shown as (1)–(3),[32] respectively,

$$q_t = q_e(1 - e^{-kt}) \quad (1)$$

$$q_t = \frac{q_e v_0 t}{q_e + v_0 t} \quad (2)$$

$$q_t = \frac{1}{b}\ln(a \times b \times t) \quad (3)$$

Table 2 presents the kinetic parameters deduced from fitting the three models to experimental data, including the q_t (mg g^{-1}) value, the k (min^{-1}) value of the pseudo-first-order kinetic model, the v_0 (μg g^{-1} min^{-1}) value of the pseudo-second-order kinetic model, and the a and b constants related to the adsorption rate.

In order to verify the existence of intermolecular forces, DFT calculations have been used to elucidate complex host-drug interactions and provide scientific guidance for drug design and optimization.[33–38] At first, utilizing independent gradient model (IGM) analysis, we were able to thoroughly investigate the topological features of the electron charge density (ρ) of the

Table 2 Kinetic parameters for the adsorption of Cur on NH_2-UiO-66 at room temperature and an initial concentration of 400 μg mL^{-1}

Models	Parameters	
Pseudo-first-order kinetic model	Q_e	177.8
	k_1	0.21
	R^2	0.99
Pseudo-second-order kinetic model	Q_e	179.0
	v_0	0.13
	R^2	0.99
Elovich model	A	6.39
	B	0.35
	R^2	0.99

system. As illustrated in Fig. 3a, the three-dimensional (3D) IGM isosurface is presented. This cluster structure is derived from the DFT-optimized periodic structure (Fig. 3b), wherein blue denotes the region of non-covalent interactions between the adsorbate and the adsorbent. Furthermore, the simulation results indicate that the model drug molecules can be successfully incorporated into the MOF and the adsorption energy is negative, with a value of −2.95 eV per unit cell, signifying that these adsorption processes are spontaneous and possess excellent thermal stability. Concurrently, it is also demonstrated that the Cur molecules are retained within the pores through attractive interactions.

Compared with the binding energy of UiO-66 synthesized by the same method (−0.68 eV),[39] that of NH_2-UiO-66 is notably lower. This difference may be attributed to the intricacy of its framework, which features high porosity and a pore size comparable to that of drug molecules. Such features enable the accommodation of guest molecules, leading to a closer distance between the adsorbent and the frame. Consequently, the intermolecular hydrogen bond length formed is shorter, the bond energy is higher, and the adsorbed crystal structure is more stable.[30] The two types of hydrogen bonds (Fig. 3c), N–H···O (1.94 Å, and 2.22 Å) and O–H···O (2.74 Å), further illustrate that the nanoparticles exhibit superior stability and a higher drug loading rate.

In addition, to clarify the inhibitory effect of nanoparticles on CFs, the CCK-8 method was used to determine the cytotoxicity of different concentrations of NH_2-UiO-66 on normal CF cells. The results showed that NH_2-UiO-66 had no significant cytotoxic effect on CF cells after 24 h of treatment (Fig. 4).

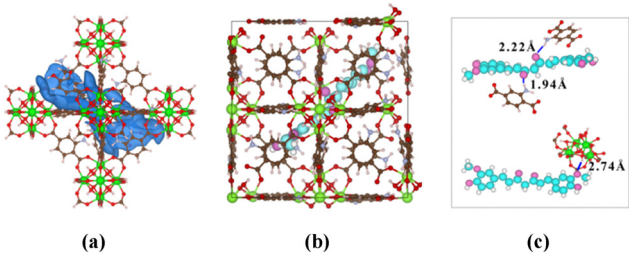

Fig. 3 (a) 3D IGM isosurface. (b) Hydrogen bond between the adsorbed Zr–O–H and the carbonyl group of Cur. (c) The hydrogen bond between the nitrogen of $-NH_2$ in NH_2-UiO-66 and the carbonyl group of Cur.

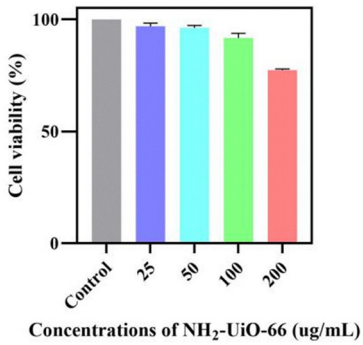

Fig. 4 The viability of CF cells at different concentrations of NH_2-UiO-66.

3.2 Protective effect of nanoparticles by regulating myocardial fibrosis in ISO-induced Balb/c mice models

Myocardial fibrosis refers to the excessive accumulation of the extracellular matrix in myocardial tissue, which is a pathological state that leads to impaired myocardial systolic and diastolic function. Continuous fibrosis can lead to arrhythmia, myocardial infarction and heart failure. Echocardiography, a non-invasive method, is used to evaluate cardiac function in mice. To further evaluate the *in vivo* therapeutic effect of nanoparticles against myocardial fibrosis, mice were divided into Sham group, ISO group, ISO + NH_2-UiO-66@Cur group, and ISO + NH_2-UiO-66@Cur@PCM group to determine the LVEF, LVFS, LVIDd and LVIDs (Fig. 5a). The results showed that ISO-induced LVEF and LVFS decreased (Fig. 5b and c), while LVIDs and LVIDd increased in Balb/c mice (Fig. 5d and e), suggesting that LVEF decreased and left ventricular systolic function decreased. The results demonstrate that the animal models were successfully developed. Following nanoparticle therapy, the levels of LVEF and LVFS in mice were considerably

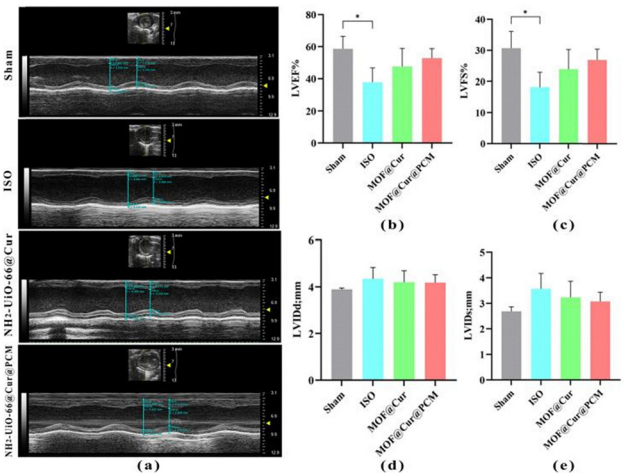

Fig. 5 The M-mode echocardiographic in experimental mice were evaluated. (a) Typical echocardiographic images. (b, c) LVEF, LVFS; (d, e) LVIDd, LVIDs. All experiments were repeated three times; *$p < 0.05$ between groups as indicated.

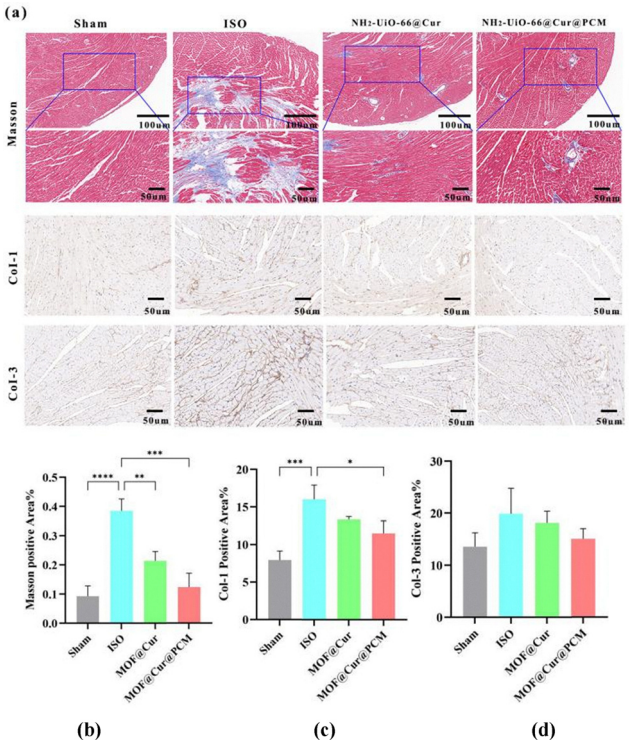

Fig. 6 (a) Cardiac fibrosis was assessed by the utilization of Masson staining, and the expression of Col-1 and Col-3 in the Sham, ISO, ISO + NH_2-UiO-66@Cur, and ISO + NH_2-UiO-66@Cur@PCM groups was determined by immunohistochemistry; (b) statistical analysis of the myocardial fibrosis area of each group; (c) and (d) statistical analysis of Col-1 and Col-3 expression. The experiments were independently performed three times, respectively; *$p < 0.05$, **$p < 0.01$, ***$p < 0.001$, and ****$p < 0.0001$ between groups as indicated.

higher than those in the model group. Conversely, no marked differences were observed in LVIDd and LVIDs between the two groups. The left ventricular function of the drug-induced operation group was still compensated, suggesting that the NH_2-UiO-66@Cur@PCM treatment group could significantly improve diastolic dysfunction. Thus, the employment of specifically targeted nanoparticles demonstrates superior potential in enhancing cardiac function. This is mainly attributed to the synergistic effect of the active targeting of peptides and the enhanced permeability and retention (EPR) effect of ischemic heart tissue, which increase drug accumulation.

The distribution of collagen deposition in the heart tissue of ISO-induced Balb/c mice was studied by Masson staining of paraffin-embedded heart tissue (Fig. 6a). A significant disruption in myocardial fiber arrangement, marked inflammatory cell infiltration, and a substantial proliferation of collagen fibers were observed. Following the administration of nanoparticles, the targeted group demonstrated limited inflammation and collagen deposition within the left ventricular (LV) region, as identified by the modest area of blue staining. Furthermore, the myocardial fibers appeared organized and orderly, suggesting a lower presence of scar tissue when compared with the model group and the non-targeted group (Fig. 6b). Through immunohistochemical examination, a significant increase of Col-1 and Col-3 expression within mouse heart tissue was observed following ISO treatment (Fig. 6c). However, the expression levels of both NH_2-UiO-66@Cur and NH_2-UiO-66@Cur@PCM groups were notably lower than those in the ISO group (Fig. 6d), indicating that the targeted group exhibited a superior therapeutic effect.

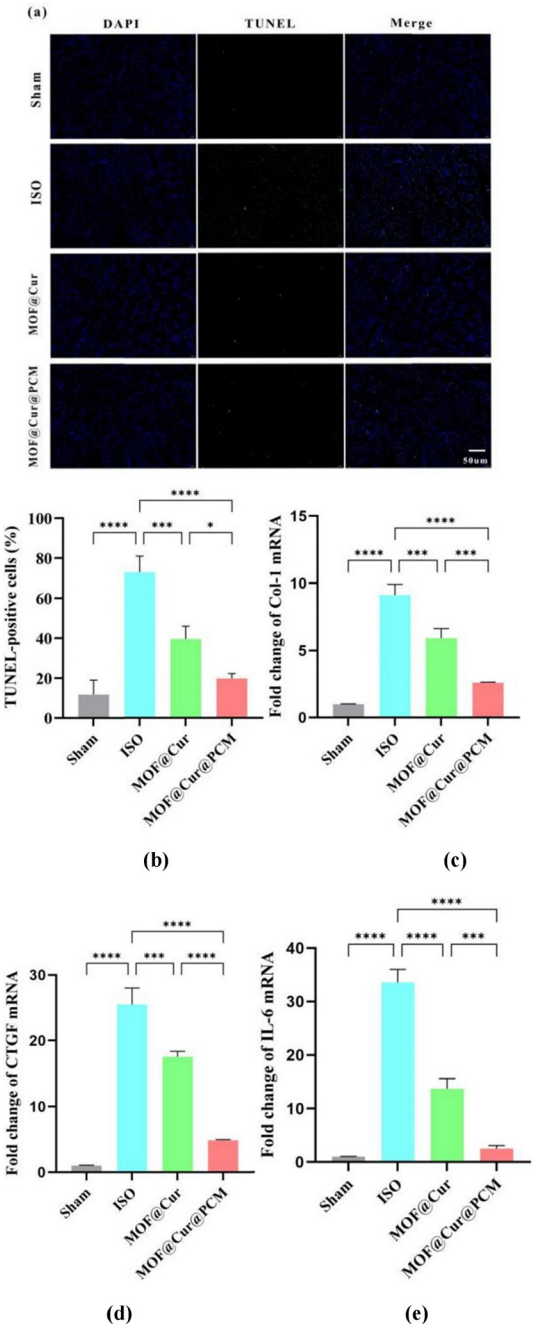

Fig. 7 (a) The myocardial tissues were subjected to TUNEL staining. (b) Statistical analysis was conducted on the apoptotic cardiomyocyte percentage (TUNEL-positive cells) of each treatment group. (c)–(e) Statistical analysis of the mRNA levels of fibrosis markers Col-1, CTGF, and IL-6 by RT-qPCR. β-actin was used as an internal loading control. The experiments were independently performed three times; *$p < 0.05$, **$p < 0.01$, ***$p < 0.001$, and ****$p < 0.0001$ between groups as indicated.

The model mice were subjected to the TUNEL assay for the detection of drug-induced cardiomyocyte apoptosis (Fig. 7a). And there was a notable increment in the prevalence of cardiomyocyte apoptosis within the model group, in comparison to the sham group. However, the treatment with the nano-drug provided a notable decrease in cardiomyocyte apoptosis (Fig. 7b). Furthermore, RT-qPCR analysis demonstrated that the expression level of two myocardial fibrosis genes and one inflammatory gene, including Col-1, CTGF, and IL-6, was significantly reduced following nanoparticle treatment when compared to the ISO group (Fig. 7c–e). These findings suggest that Cur possesses anti-fibrotic properties for isoproterenol-induced cardiac remodeling, which is consistent with previous studies.[40–42] The compelling implications derived from these comprehensive, long-term investigations indicate that the intracytoplasmic injection of targeted drug-laden nanoparticles can effectively preserve cardiac function by promoting the survival of cardiomyocytes and curtailing the progression of pathological myocardial remodeling.

4. Conclusions

To sum up, we successfully developed a novel targeted nano-drug delivery system (NH_2-UiO-66@Cur@PCM) integrating active targeting and the EPR effect, providing a promising strategy for myocardial fibrosis treatment. By combining precise atomic-level structural design with DFT calculations, we systematically elucidated the host–guest interaction mechanism between MOFs and Cur, while validating its therapeutic efficacy in a mouse model of myocardial fibrosis. These findings not only advance the application of MOFs in biomedicine but also open new avenues for developing innovative therapeutic strategies for cardiovascular diseases.

Author contributions

Jiao Liu: funding acquisition, conceptualization, data curation, formal analysis, and writing – original draft. Xueli Zhao: data curation and methodology. Bo Wang: investigation, methodology, and software. Ruoxuan Li: investigation and methodology. Yuze Qin: investigation and methodology. Yue Wang: investigation and methodology. Jia Zhao: investigation and methodology. Lanlan Zhang: investigation and methodology. Liang Yu: conceptualization, funding acquisition, project administration, and supervision. Liwen Liu: conceptualization, funding acquisition, project administration, and supervision.

Conflicts of interest

There are no conflicts to declare.

Data availability

The data supporting the findings of this study are available within the article. Requests for access to additional data should be directed to the corresponding author.

Acknowledgements

This work was supported by the NSFC (82202169, 82001831, 82371974, and 82071932) and the Xijing Hospital Medical Personnel Training Propel Project (XJZT24CY04).

References

1 Y. Han, T. Yan, H. Li, S. Chen, Z. Zhang, M. Wang, M. Chen, Y. Chen, X. Yang, L. Wei, Y. Duan and S. Zhang, *Acta Pharmacol. Sin.*, 2024, **0**, 2567–2578.
2 W. Javed, A. Malhotra and P. Swoboda, *Int. J. Cardiol.*, 2024, **394**, 131382.
3 X. Chen, H. Chen, L. Zhu, M. Zeng, T. Wang, C. Su, G. Vulugundam, P. Gokulnath, G. Li, X. Wang, J. Yao, J. Li, D. Cretoiu, Z. Chen and Y. Bei, *ACS Nano*, 2024, **18**, 19470–19488.
4 W. Rao, D. Li, Q. Zhang, T. Liu, Z. Gu, L. Huang, J. Dai, J. Wang and X. Hou, *J. Transl. Med.*, 2025, **23**, 1–17.
5 M. Long, L. Wang, L. Kang, D. Liu, T. Long, H. Ding, Y. Duan, H. He, B. Xu and N. Gu, *ACS Nano*, 2025, **19**(4), 4561–4581.
6 Y. Zhu, F. Zhang, Z. Li, Y. Zhou, Y. Shu, J. Ruan and G. Chen, *Front. Cardiovasc. Med.*, 2025, **11**, 1477601.
7 F. Lv, H. Yin, Y. Q. He, H. Wu, J. Kong, X. Chai and S. R. Zhang, *Exp. Ther. Med.*, 2016, **12**, 3877–3884.
8 S. Bazzazan, K. Moeinabadi-Bidgoli, Z. A. Lalami, S. Bazzazan, M. Mehrarya, F. E. Yeganeh, F. Hejabi, I. Akbarzadeh, H. Noorbazargan, M. Jahanbakhshi, N. Hosseinkhannazer and E. Mostafavi, *J. Drug Deliv. Sci. Technol.*, 2023, **79**, 104009.
9 P. Anand, A. B. Kunnumakkara, R. A. Newman and B. B. Aggarwal, *Mol. Pharm.*, 2007, **4**, 807–818.
10 J. Liang and B. Liu, *Bioeng. Transl. Med.*, 2016, **1**, 239–251.
11 P. M. Boarescu, I. Boarescu, I. C. Bocsan, R. M. Pop, D. Gheban, A. E. Bulboaca, C. Nicula, R. M. Rajnoveanu and S. D. Bolboaca, *Molecules*, 2019, **24**, 2802.
12 J. Liu, J. Xue, G. Yang, L. Dang, L. Ma, D. Li and Y. Wang, *Coord. Chem. Rev.*, 2022, **463**, 214521.
13 H. Yang, J. Liu, L. Wang, L. Ma, F. Nie and G. Yang, *Talanta*, 2022, **238**, 123041.
14 X. Zhao, X. Wang, J. Wang, J. Yuan, J. Zhang, X. Zhu, C. Lei, Q. Yang, B. Wang, F. Cao and L. Liu, *Int. J. Nanomed.*, 2020, **15**, 1321–1333.
15 J. Guo, Z. Yang, Y. Lu, C. Du, C. Cao, B. Wang, X. Yue, Z. Zhang, Y. Xu, Z. Qin, T. Huang, W. Wang, W. Jiang, J. Zhang and J. Tang, *Bioact. Mater.*, 2022, **10**, 56–67.
16 P. J. Jodlowski, G. Kurowski, L. Kuterasinski, M. Sitarz, P. Jelen, J. Jaskowska, A. Kolodziej, A. Pajdak, Z. Majka and A. Boguszewska-Czubara, *ACS Appl. Mater. Interfaces*, 2021, **13**, 312–323.
17 Z. Wang, N. Yang, Y. Hou, Y. Li, C. Yin, E. Yang, H. Cao, G. Hu, J. Xue., J. Yang and Z. Li, *Adv. Sci.*, 2023, **10**, 2302123.

18 H. Weng, W. Zou, F. Tian, H. Xie, A. Liu, W. Liu, Y. Liu, N. Zhou, X. Cai, J. Wu, Y. Zheng and X. Shu, *Nat. Commun.*, 2024, **15**, 6058.
19 J. Wang, E. Lukse, A. Seth and C. A. G. McCulloch, *Tissue Cell.*, 2001, **33**, 86–96.
20 Y. Qiu, X. Song, Y. Liu, Y. Wu, J. Shi, F. Zhang, Y. Pan, Z. Cao, K. Zhang, J. Liu, Y. Chu, X. Yuan and D. Wu, *Appl. Microbiol. Biotechnol.*, 2023, **107**, 6251–6262.
21 H. Fu, B. Kong, W. Shuai, J. Zhu, X. Wang, Y. Tang, H. Huang and C. Huang, *Heart Rhythm*, 2024, **21**, 1998–2009.
22 X. Zhao, W. Luo, J. Hu, L. Zuo, J. Wang, R. Hu, B. Wang, L. Xu, J. Li, M. Wu, P. Li and L. Liu, *Nanobiotechnology*, 2018, **16**, 36.
23 P. Hohenberg and W. Kohn, *Phys. Rev.*, 1964, **136**, B864.
24 G. Kresse and J. Furthmüller, *Phys. Rev. B: Condens. Matter Mater. Phys.*, 1996, **54**, 11169.
25 J. Perdew, K. Burke and M. Ernzerhof, *Phys. Rev. Lett.*, 1996, **77**, 3865–3868.
26 S. Grimme, J. Antony, S. Ehrlich and H. Krieg, *J. Chem. Phys*, 2010, **132**, 154104.
27 T. Lu and F. Chen, *J. Comput. Chem.*, 2012, **33**, 580–592.
28 P. Fotouhi, S. Sohrabi, N. Nosrati, A. Z. Vaziri, S. Khaleghi, A. Narmani, H. Jafari and J. Mohammadnejad, *Process Biochem.*, 2021, **111**, 221–229.
29 A. Narmani, M. Rezvan, B. Farhood, P. Darkhor, J. Mohammadnejad, B. Amini, S. Refahi and N. G. Abdi, *Drug Dev. Res.*, 2019, **80**, 404–424.
30 Z. Zhang, C. Tao, J. Zhao, F. Wang, J. Huang and J. Wang, *Catalysts*, 2020, **10**, 1086.
31 H. Molavi, M. Zamani, M. Aghajanzadeh, H. K. Manjili, H. Danafar and A. Shojaei, *Appl. Organomet. Chem.*, 2018, **32**, e4221.
32 J. Li, L. Liang, H. Zhou, P. Zhang, Z. Kong and X. Duan, *Z. Anorg. Allg. Chem.*, 2022, **649**, e202200261.
33 Y. Gao, K. Liu, R. Kang, J. Xia, G. Yu and S. Deng, *J. Hazard. Mater.*, 2018, **359**, 248–257.
34 M. N. Ansari, U. Bhandari and K. K. Pillai, *Hum. Exp. Toxicol.*, 2007, **26**, 933.
35 Y. Wang, J. Wang, C. Liu, J. Li, K. Lu, Q. Yu, Y. Zhang and Z. Shen, *J. Mater. Sci. Technol.*, 2023, **167**, 50–58.
36 L. Li, Y. Zhu, Z. Qi, X. Li, H. Pan, B. Liu and Y. Liu, *Appl. Organomet. Chem.*, 2023, **37**, e7199.
37 H. Song, Y. Cai, L. Nan, J. Liu, J. Wang, X. Wang, C. Liu, J. Guo and L. Fang, *ACS Appl. Mater. Interfaces*, 2024, **16**, 9799–9815.
38 X. Deng, W. Wu, S. Tian, Y. He, S. Wang, B. Zheng, K. Xin, Z. Zhou and L. Tang, *Chem. Eng. J.*, 2024, **479**, 147634.
39 F. Edi-Soetaredjo, M. Slama, L. Sellaoui, H. Ghalla, M. B. El Hadj Rhouma, S. Ismadji and B. Ernst, *Chem. Eng. J.*, 2023, **474**, 145633.
40 C. A.Anyama, H. Louis, B. E. Inah, T. E. Gber, J. O. Ogar and A. A. Ayi, *J. Mol. Struct.*, 2023, **1277**, 134825.
41 C. Jiang, Q. Shi, J. Yang, H. Ren, L. Zhang, S. Chen, J. Si, Y. Liu, D. Sha and B. Xu, *J. Adv. Res.*, 2024, **63**, 159–170.
42 Y. Thi Dang, H. T. Hoang, H. C. Dong, K. T. Bui, L. H. T. Nguyen, T. B. Phan, Y. Kawazoe and T. L. H. Doan, *Microporous Mesoporous Mater.*, 2020, **298**, 110064.